The Effect of γ'' and δ Phase Precipitation on the Mechanical Properties of Inconel 718 Manufactured by Selective Laser Melting: An In Situ Neutron Diffraction and Acoustic Emission Study

JAN ČAPEK [1,7] EFTHYMIOS POLATIDIS,[1] MICHAL KNAPEK,[2,3]
CHRISTOPHE LYPHOUT,[4] NICOLA CASATI,[5] ROBERT PEDERSON,[6]
and MARKUS STROBL[1,3]

1.—Laboratory for Neutron Scattering and Imaging, Paul Scherrer Institute, 5232 Villigen-PSI, Switzerland. 2.—Faculty of Mathematics and Physics, Charles University, 121 16 Prague, Czech Republic. 3.—Nuclear Physics Institute of the Czech Academy of Sciences, 250 68 R?ež, Czech Republic. 4.—Research Institutes of Sweden, Lindholmspiren 7 A, Göteborg 417 56, Sweden. 5.—Materials Science Group, Photon Science Division, Paul Scherrer Institute, 5232 Villigen-PSI, Switzerland. 6.—Department of Engineering Science, University West, 46132 Trollhättan, Sweden. 7.—e-mail: jan.capek@psi.ch

The deformation behavior of additively manufactured Alloy 718 in as-built condition and after annealing was studied in situ under tensile loading along the build direction. Pre-characterization by synchrotron X-ray diffraction and electron microscopy revealed a significant amount of γ'' precipitates in the as-built samples, whereas the γ'' phase was entirely consumed and needle-like δ precipitates appeared in the annealed sample. In situ neutron diffraction (ND) and acoustic emission (AE) enabled indirect observation of the role of the precipitates on the mechanical behavior. ND provided information on the load accommodation in the matrix, while AE detected a strong signal from the interaction of dislocations with the δ-phase precipitates during deformation of the annealed samples. The results imply that in the annealed samples the matrix sheds the load to the precipitates, while in the as-built material the matrix bares a significant load.

INTRODUCTION

Alloy 718 (also known as Inconel 718) is a Ni-based superalloy that is widely used for components in gas turbines in jet engines because of its good mechanical properties and corrosion resistance at elevated temperatures.[1] The good combination of strength and ductility of Alloy 718 derives from its ductile γ phase matrix with face-centered cubic (fcc) crystal structure and the coherent γ'' phase precipitates with Ni_3Nb composition and a body-centered tetragonal ($D0_{22}$) crystal structure (bct crystal structure). Less often, γ' precipitates with a face-centered cubic (fcc) crystal structure are present. The precipitation of either γ' or γ'' is dependent on the concentration of Ti and Nb.[2] Typically, Alloy 718 is used for medium-temperature applications, because above 650°C the thermodynamically stable δ phase forms, with Ni_3Nb composition and an orthorhombic ($D0_a$) crystal structure, at the expense of the γ'' phase. The appearance of δ, at the expense of the γ'', has been observed to degrade the mechanical properties of the material.[3–5] The δ phase precipitates can form either at the grain boundaries or intragranularly. A recent study showed that when δ appears at the grain boundaries in sufficient amounts, it leads to a better formability of Alloy 718, whereas δ precipitation inside the grains leads to hardening of the material.[6] Precipitation of Laves and carbide phases, which are responsible for reduced ductility.[7,8] is also commonly observed in Alloy 718.

Fabricating components of Alloy 718 using additive manufacturing (AM) methods is very attractive for many applications due to the large degree of design flexibility that they offer. One of the most commonly used AM processes is the family of so-called powder bed fusion processes, including the following methods: direct metal laser sintering (DMLS), electron beam melting (EBM), selective heat sintering (SHS), laser powder bed fusion (LPBF: frequently referred to selective laser melting, SLM), and selective laser sintering (SLS).[9] LPBF is an established method for processing metals and alloys where a laser source is utilized for melting and selectively fusing together metallic powders, which are spread by a recoater on a build plate that moves downwards as the metallic component is being built. In LPBF, the laser power, scanning speed, hatch spacing, and layer thickness are the most influential parameters and the most common process parameters adjusted to optimize the process. Hence, significant work has been undertaken to understand the link between processing parameters and produced microstructure for particular metals/alloys. For Alloy 718 specifically, a few recent examples are contained in references.[10–17] It has been observed that Alloy 718 exhibits a heterogeneous microstructure in its as-built form, containing a large amount of segregating phases, such as MC-type carbides and γ/Laves phase eutectics within the interdendritic regions.[18] Typically a two-step heat treatment process is undertaken to improve its mechanical properties: (1) solution annealing to dissolve the segregation particles and strengthening phase into the matrix, followed by (2) ageing heat treatment to precipitate fine particles of γ' or γ'' phases in the matrix.[19–23] Besides γ' and γ'' phases, δ phase forms at the grain boundaries and inside the grains, and Laves phases as well as carbides appear in the matrix during ageing.[24] Despite the significant work done on wrought 718 alloys, the complex thermal cycles and fast cooling rate of the AM processes result in different phase distributions, and grain and precipitate morphologies. As such, their effect on the mechanical behavior of these materials is still not very well understood.

The Laves, δ and carbide precipitates are usually small in size and relatively low in fraction and therefore their identification and quantification is challenging using electron microscopy methods. Moreover, due to the low symmetry of the crystal structures of Laves, δ, and carbide phases, and due to the existence of multiple diffraction peaks that overlap with the diffraction peaks of the matrix (the a lattice parameter of γ'' is about half the c lattice parameter and very close to the a lattice parameter of γ), laboratory X-ray diffraction (XRD) methods struggle to identify the phases. Thus, synchrotron XRD, due to the high flux, is essential for indexing and quantifying the existence of different phases in low fractions in the bulk of the material. The drawback of XRD is that at low energies X-rays cannot penetrate deep into the material and thus the probed volume is smaller than for ND. Due to the typically rather large grain sizes of LPBF-processed materials (in the order of tens to hundreds of microns) low-energy XRD does not provide satisfactory grain statistics. Grain statistics are significantly improved when high-energy beamlines are employed in combination with large beam size.[25,26] Neutron diffraction (ND), on the other hand, allows the investigation of large gauge volumes; but at a lower resolution which does not allow evaluation of the deformation behavior of the precipitates.

The motivation of the current work was to study the deformation behavior of Alloy 718 containing γ'' phase material in comparison with the deformation behavior of a microstructure where δ phase dominates, and γ'' is absent. The effect of texture is not the focus in this paper. The first investigated material was an as-LPBF processed Alloy 718 that contained a significant amount of γ''. The second investigated material was an LPBF-processed Alloy 718 which had been annealed at 850°C for 8 h and thus predominantly contained δ phase. The initial characterization was undertaken using synchrotron XRD, while ND was used concurrently in situ with the deformation tests. A particular focus of this work was the synergy of ND and acoustic emission (AE) for observing indirectly the effect of precipitation on the mechanical behavior under uniaxial loading. The findings were compared with previous studies undertaken on wrought materials.

EXPERIMENTAL

Tensile dogbone-shaped specimens with gauge length of 25 mm and 6 mm diameter were produced from pre-alloyed 718 powder using the parameters: 200-W laser power, 900-mm/s scanning speed, 0.12-mm hatching spacing, and 30-mm layer thickness. The loading direction of the tensile specimens corresponded with the building direction. The threads for fixing the samples on the tensile rig were machined after the LPBF fabrication.

The microstructure of the samples was characterized by electron backscattered diffraction (EBSD). The samples were ground with 4000 grit SiC paper, polished down to 0.25 μm and then electropolished using a 70-ml H_2O, 200-ml glycerol, 720-ml H_2SO_4 solution at 40 V for 30 s. A field emission gun scanning electron microscope (FEG SEM) Zeiss ULTRA 55 equipped with EDAX Hikari Camera operated at 20 kV in high current mode with a 120-μm aperture was used. The EBSD raw data was post-processed using the EDAX OIM Analysis 7.3 software.

The in situ ND experiments under uniaxial tension were carried out at the time-of-flight POLDI diffractometer[27,28] at the Swiss Spallation Neutron Source, SINQ at the Paul Scherrer Institute, Switzerland, using the tensile rig of the beamline. The samples were deformed with an initial strain

The Effect of γ'' and δ Phase Precipitation on the Mechanical Properties of Inconel 718 Manufactured by Selective Laser Melting: An In Situ Neutron Diffraction and Acoustic Emission Study

225

rate of 4×10^{-4} s^{-1} in displacement control. The strain was measured with a mechanical extensometer attached to the sample. The ND measurements were undertaken upon stopping the tensile experiment and holding the strain at predefined strain positions. A gauge volume of $3.8 \times 3.8 \times 3.8$ mm^3 was defined by a pair of diaphragms in the incident beam and a radial collimator on the diffracted beam. The obtained data were fitted using a Gaussian function in Mantid[29] to obtain the peak position and full width at half maximum (FWHM).

Three samples for each condition were tested in total. Two deformation measurements in displacement control mode were performed together with ND with the loading direction being parallel or perpendicular to the scattering vector, hereafter denoted as BD and TD respectively. ND data were collected at predefined strain intervals after interrupting the loading and holding the displacement for 65 min and 40 min for BD and TD measurements, respectively. A 3-min waiting time was applied to allow for stress relaxation before the ND measurements started. Since the interpretation of TD data is not straightforward, we focus mainly on the interpretation of BD data.

A third measurement was undertaken with the AE system attached to the sample during continuous tensile tests. AE was measured using the Vallen AMSY-6 multi-channel system with an ASIP-2 AE signal processor. A Vallen AEP5 preamplifier (40 dB) and Physical Acoustic Corporation (PAC) Micro 30S sensor were used. The sensor was attached directly to the sample with the help of a plastic clip. Vacuum grease (Apiezon M) was employed to facilitate better acoustic contact between the sensor and the sample. The AE count rate (AE counts per second) was evaluated based on the threshold-level AE detection, with the threshold set at 24 dB.

For the synchrotron XRD investigations, thin strips of material were cut from the samples and mechanically ground (using SiC papers 1200-2500-4000 grit) and polished (using a 1-μm diamond suspension) down to a thickness of approximately 100 μm. At this thickness any residual stress (RS) present in the as-built material is expected to be relaxed. Synchrotron XRD measurements were undertaken at the MS beamline of the Swiss Light Source (SLS) at the Paul Scherrer Institute, Switzerland using a 25-keV beam and a 70×70 μm^2 spot size. The measurements were performed in transmission using a Pilatus 6 M detector to capture the entire Debye–Scherrer rings. Several points were measured, but they did not exhibit significant differences in terms of precipitation. The diffraction data were calibrated using a LaB$_6$ NIST SRM 660b and integrated along the entire azimuthal range using the open source software bubble.[30] After indexing of the diffraction patterns, Rietveld refinement was carried out using the open access software GSAS-2 for obtaining the phase fractions of the constitutive phases.[31]

The raw 2D diffraction pattern is shown in Fig. 1a. One can see that the diffraction pattern does not form full circles but rather individual spots. This is due to the small number of grains in the diffraction volume. Such a pattern is not suitable for in situ investigations due to the relatively poor diffraction grain statistics, i.e., the grain size of the principal phase, γ, is in the order of 30 μm. The angular integration of the XRD pattern is shown in Fig. 1b and compared with ND data. It is obvious that the signal to background noise ratio is much higher for XRD than for ND, while the peaks from precipitates are beyond the resolution of ND.

RESULTS AND DISCUSSION

The as-LPBF processed and the heat-treated material contained different phases, as revealed by the Rietveld refinement of the XRD data shown in Fig. 2. For both samples, the Rietveld refinement gives a good fit to the experimental data and it was observed that the as-built specimen contained a mixture of matrix γ phase with $20.4 \pm 0.8\%$ of γ'' phase, $1.8 \pm 0.1\%$ of Laves phases, and $0.2 \pm 0.1\%$ of metallic carbides, whereas no δ phase peaks were found. After annealing at 850°C for 8 h, the γ'' phase disappeared, which is seen as a vanishing of the peak "shoulder" shown in the diffraction pattern of the as-built material, i.e., the (111) and (200) peaks of the γ matrix become sharper, as shown in Fig. 2b, and γ'' is not included in the Rietveld fitting. On the other hand, the volume of δ phase increases to $11.8 \pm 0.6\%$, the Laves phases to $6.1 \pm 0.9\%$, and the metallic carbides to $0.8 \pm 0.5\%$. The δ phase precipitates accumulated along the grain boundaries and needle-like δ phase precipitates were distributed inside the grains, as shown in the backscattered-electron (BSE) SEM image in Fig. 3a and 3b which is in good agreement with the microstructure of Alloy 718 annealed at 980°C.[32,33] The carbides are seen as dark spots in the BSE mode in Fig. 3b as previously also reported in Ref. 15 The as-built material exhibits a characteristic dendritic structure and a relatively high fraction of bright dendrite boundaries are observed in the BSE micrographs, which implies heavy element segregation, i.e., Nb-rich precipitates.[34] Based on the phase fraction obtained by Rietveld analysis, these precipitates can only be γ'' phase (i.e., 20.4% in fraction), which has been shown to be rich in heavy elements.[35] This observation is in contrast with previous observations where a high fraction of Laves phases where observed at the dendrite boundaries;[19,36] the Laves phase fraction of the as-built material of the present work was only 1.8%.

The true stress–strain curves are shown in Fig. 4 for both materials. There was a good agreement between the in situ and ex situ tests; therefore, only the continuous deformation curve is shown in Fig. 4. The as-built material exhibits remarkable mechanical properties, due to the presence of a
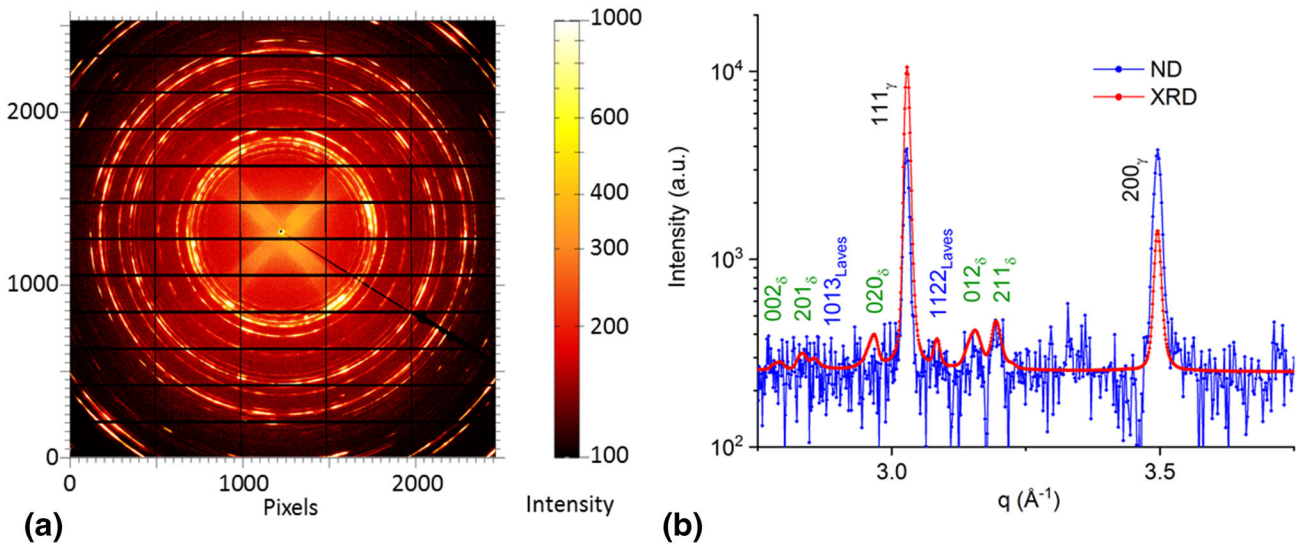
Fig. 1. (a) 2D XRD pattern. (b) Comparison of ND and XRD patterns in a section.
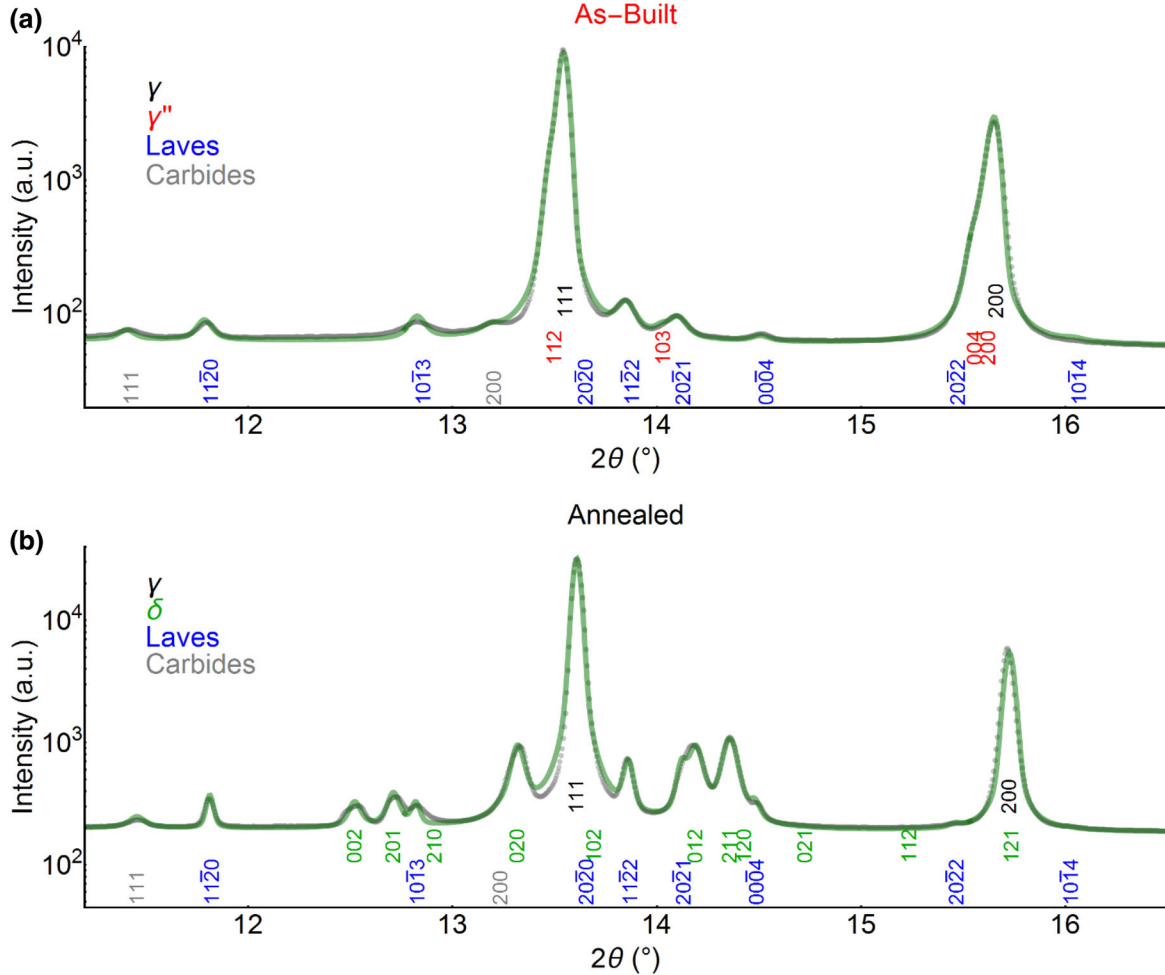

Fig. 2. Synchrotron XRD patterns (*points*) and Rietveld refinement pattern (*green line*) for (a) as-built, and (b) annealed specimen.

significant amount of γ'', which are comparable with the mechanical properties obtained after 2-step annealing treatment in LPBF-processed materials

reported in Ref. 37. Annealing at 850°C for 8 h increases the strength significantly and reduces the ductility of the material. The change in the

mechanical properties is associated with the different fraction and type of precipitation between the two materials. As discussed above, fine δ particles form in the grain interior (cf. Fig. 3), typically upon annealing at temperatures below 900°C.[6] The presence of these δ particles in the annealed specimen strengthens the material and results in a pronounced work-hardening rate during the initial stage of plastic deformation compared with the as-built sample, as shown in Fig. 5. The mechanical properties of the two materials are summarized in Table I.

Both materials exhibit very strong AE activity in the beginning of loading in the apparent elastic stage of deformation (Fig. 4). It is generally believed that elastic deformation of metals does not lead to AE as it does not involve generation of energy bursts within the sample, which is typical for plastic deformation (e.g., dislocation avalanches, mechanical twinning, cracking etc.).[38] It is therefore apparent that the initial deformation is not ideally elastic in these materials and that some localized sources of AE are activated before reaching the macroscopic yield point. It was shown that very fine oxides

(mostly Al_2O_3) form in the Inconel 718 alloy during SLM processing.[39] These brittle oxide particles have relatively low tensile strength[40] together with higher elastic modulus than the matrix, 330 GPa and 200 GPa, respectively; they break during the macroscopic elastic loading, thus giving rise to AE. Note that the total volume of these particles is typically lower than 0.1% in SLM-processed Inconel 718, which is below the detection limit of the XRD analysis (Fig. 2). Similarly, the formation of these particles does not considerably affect the inherent precipitation sequence of this material.[39]

The AE activity reaches its maximum near the macroscopic yield point in both materials. This feature is characteristic of fcc metals and reflects massive dislocation activity (and possible twinning) as the material starts to deform plastically.[38,41,42] During the later stages of deformation the AE response gradually diminishes. This observation is related to reduced mean free path of dislocations due to the formation of dislocation entangles, forest dislocations, and new high-angle grain boundaries (a result of twinning) as the materials harden.[38] Moreover, Alloy 718 generally has a relatively low
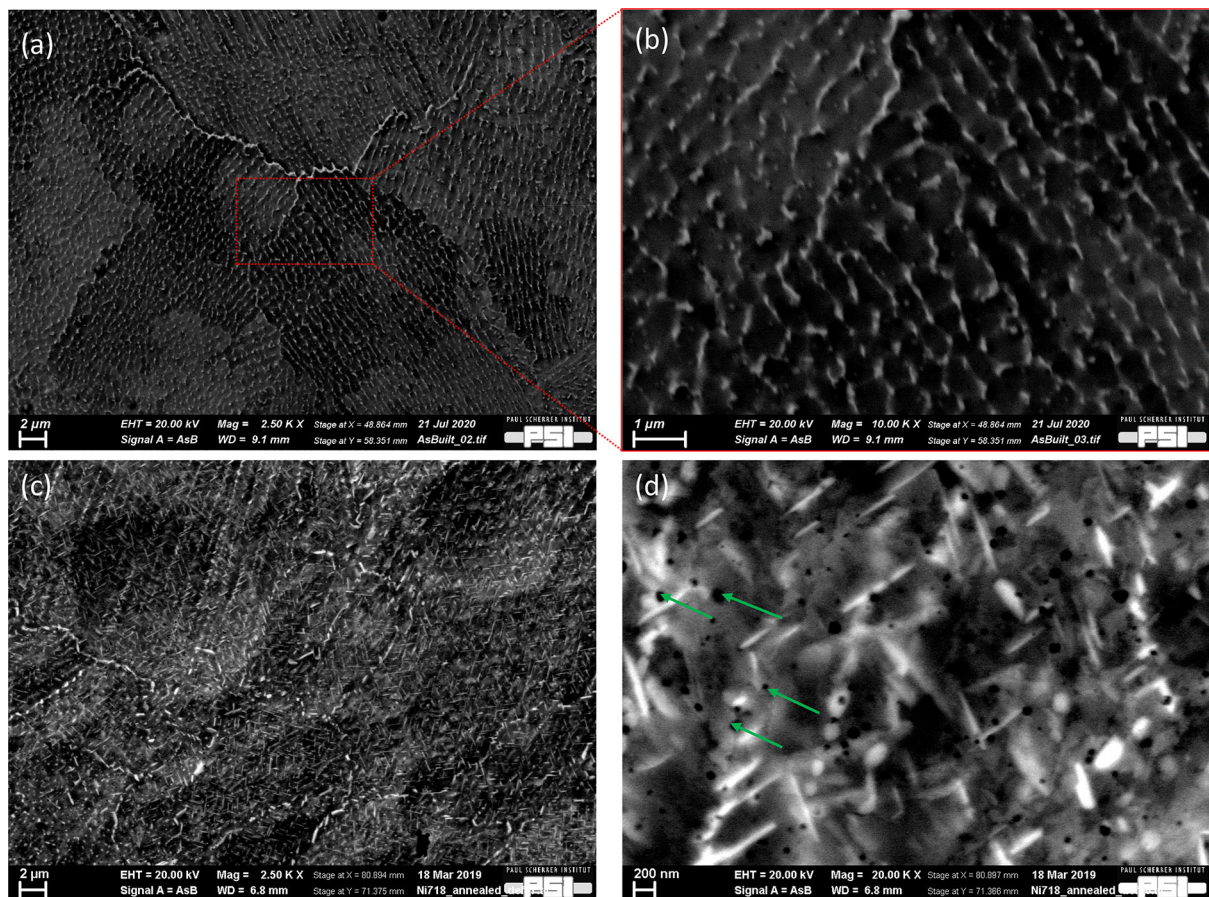

Fig. 3. (a) Low and (b) higher magnification backscattered SEM image of the as-built sample showing the dendritic structure and elemental segregation of heavy elements at the dendrite boundaries due to precipitation of γ''. (c) Low magnification backscattered SEM image of the annealed sample showing the presence of needle-like δ phase at the grain boundaries and inside the grains. (d) High magnification backscattered SEM image showing the needle-like δ phase and carbides (dark spots shown with green arrows).
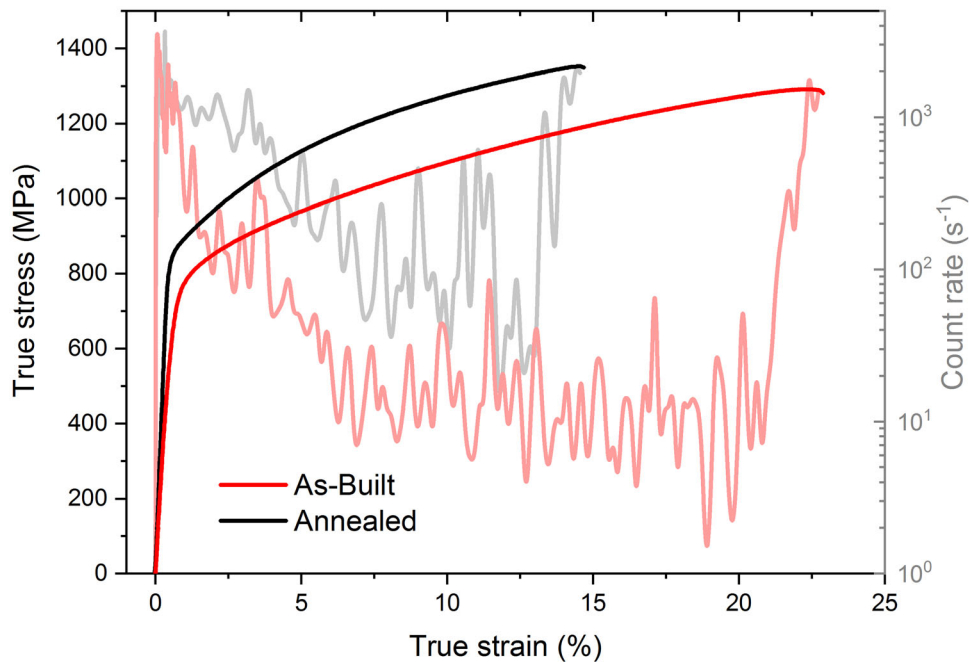
Fig. 4. True stress–strain curve for the as-built and annealed sample and AE count rate; data from the continuous deformation test.

stacking fault energy and a high modulus of elasticity. In such materials, dislocation cross-slip is typically difficult.[43]

Figure 4 also shows that, although qualitatively similar, a much stronger AE response was observed in the aged sample in the latter stages of deformation. This is due to the different strengthening effect of precipitates. The presence of γ'' precipitates has been associated with coherency hardening[44,45] where the dislocations cut through the precipitates, introducing stacking faults and antiphase boundaries in the precipitates.[46,47] The presence of δ phase has been shown to inhibit the dislocation movement during deformation[48,49] and dislocations pile up in the vicinity of the precipitates, which act as breakable pins. With increasing stress, energetic dislocation avalanches occur as they overcome the precipitates, thus giving rise to strong AE signals.[38] Hence the annealed sample exhibits strong AE activity during loading due to the possibility of cross-slip. A corresponding observation for a similar Ni-based superalloy was reported in Ref. 50.

Figure 5 shows the lattice strain evolution for the 111_γ, 200_γ, 311_γ, and 220_γ grains aligned with the loading direction for both materials, together with the deformation curve and work hardening. The {111} lattice plane family is the stiffest elastically, while the {200} is the most compliant. This is typical for Ni single crystals[51] and it was also observed in various fcc materials with mild texture or when intragranular strains are not strong.[52] The work hardening before the yield point of the annealed sample is flat, showing perfect elastic behavior. The as-built sample, on the other hand, exhibits a slight decrease in work hardening, which can be

attributed to the presence of steep residual stresses in the as-built material. The presence of steep RS affects the evolution of peak broadening during the deformation, which is shown in Fig. 6 and discussed in the following paragraphs. The macroscopic yield stress of the as-built specimen is ~ 714 MPa and at this stress the elastic strain deviates from linearity for all lattice plane families, which is indicative of the onset of plastic deformation, as shown in Fig. 5a. At applied stresses higher than the yield point, the {111} and {220} lattice plane families shed load to the {200} family, which takes up significant elastic load. The {311} planes deviate from linear behavior only slightly, exhibiting the average elastic response of the sample. This suggests that the γ matrix fulfills the stress equilibrium and the γ'' precipitates do not carry significant load. At the onset of the macroscopic plastic deformation of the annealed specimen, all lattice plane families appear to shed load, which is seen as an abrupt change of the lattice strain evolution in Fig. 5b. A sharp change in the work hardening is also observed and correlates with the kink of the lattice strain. A previous investigation on Alloy 718[53] showed that the δ phase bears significantly higher load than the γ matrix, and therefore the observed deviation of the lattice strain in γ and work hardening is possibly due to γ matrix shedding load to the δ phase. This observation is in good agreement with high-temperature deformation investigations of δ-containing Ni superalloys. It was shown that dislocation entangles occur in the vicinity of δ-phase particles, which considerably contribute to the work hardening.[48,54,55]

The Effect of γ'' and δ Phase Precipitation on the Mechanical Properties of Inconel 718 Manufactured by
Selective Laser Melting: An In Situ Neutron Diffraction and Acoustic Emission Study
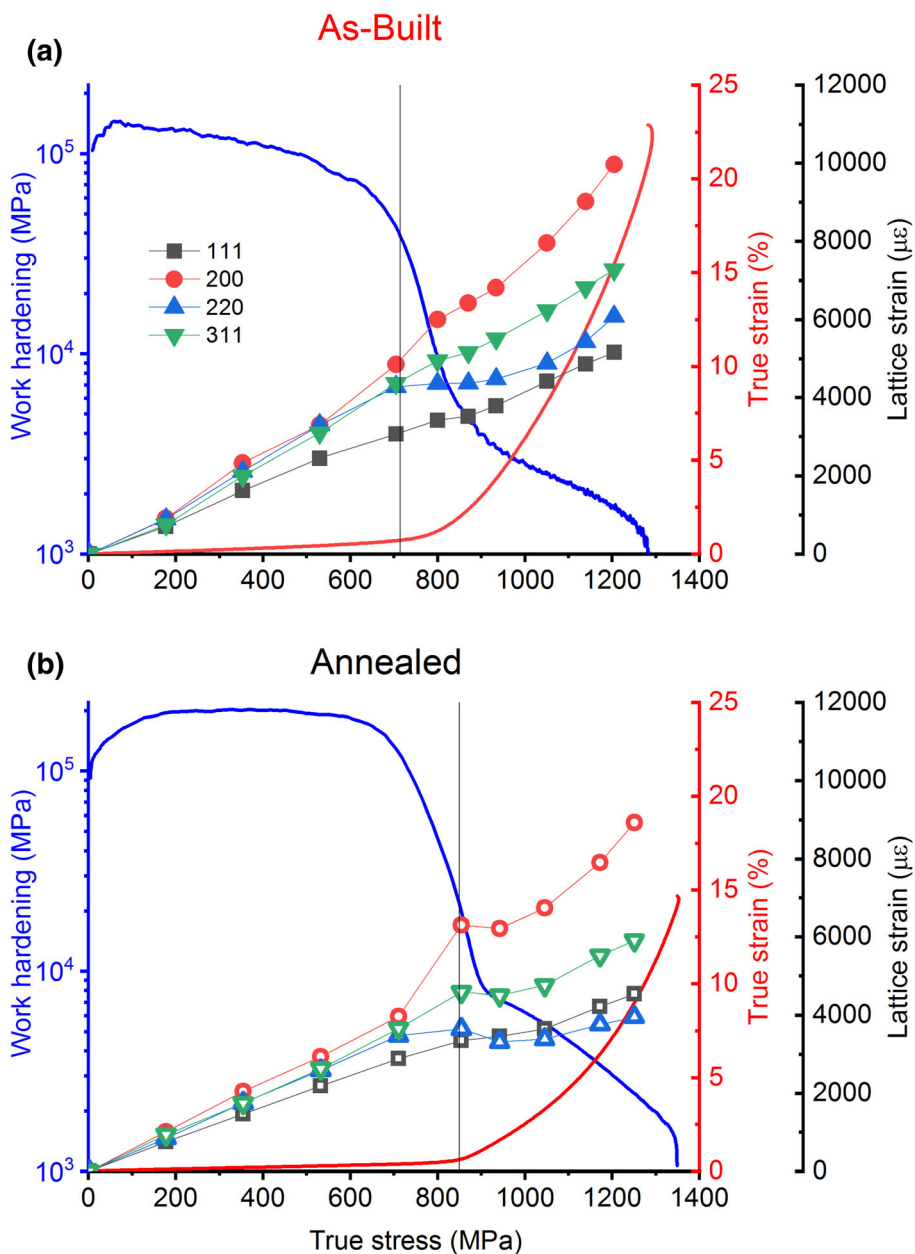
229

Fig. 5. Lattice strain with stress curves for the {111}, {200}, {220}, and {311} lattice plane families along the loading direction shown together with work hardening for (**a**) the as-built specimen and (**b**) the annealed specimen.

Table I. Summary of the tensile properties for Alloy 718 processed by LPBF in the as-built and annealed (850°C for 8 h) conditions

Sample	Yield strength, $\sigma_{0.2}$, MPa	Young's modulus, E, GPa	Tensile strength, σ_{UTS}, MPa	Fracture strain, ε_{f}, %
As-built	714	202	1290	22.3
Annealed	850	138	1350	14.5
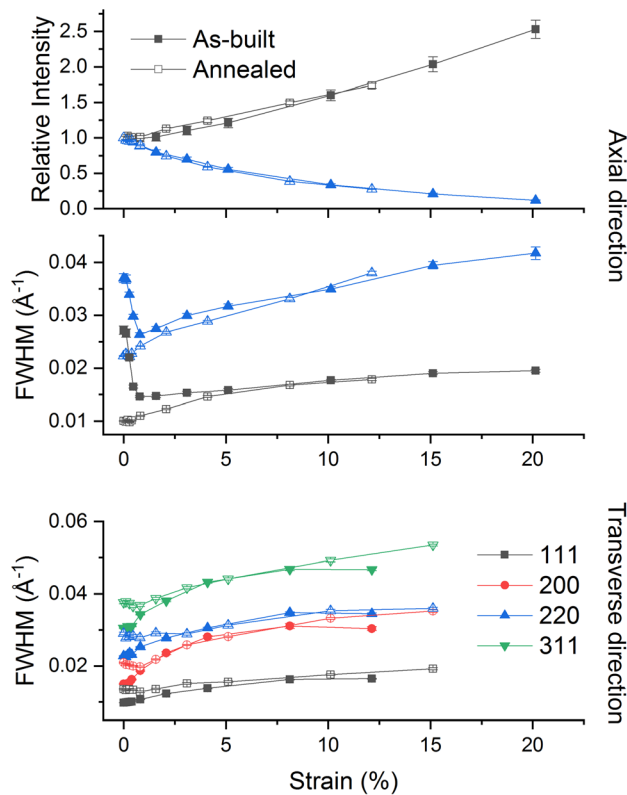
Fig. 6. Evolution of the FWHM and integrated intensity of selected peaks for the as-built and annealed specimens.
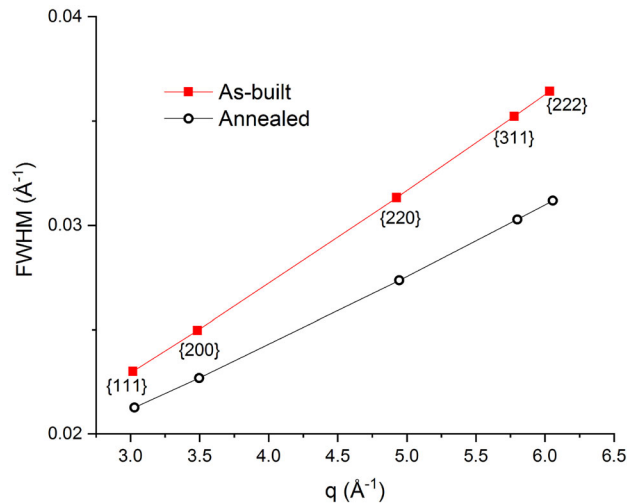
Fig. 7. FWHM for several diffraction peaks for the as-built and annealed specimens, evaluated from the XRD data.

Using the data from XRD (Fig. 2), where no RS are present due to the small sample thickness, the dislocation broadening is slightly higher in the as-built sample, as shown in Fig. 7, since the dislocations were partly recovered during annealing. It is expected that broadening predominantly depends on the dislocation activity. However, the higher broadening in ND in the initial state of deformation

of the as-built sample cannot be explained only by dislocation broadening (Fig. 6). The LPBF process is known to create a relatively high RS and steep RS gradient close to the surface of the sample.[56,57] Due to the large gauge volume of ND, areas with different magnitude and even sign of RS are sampled; therefore, variable lattice spacing is sampled and hence broad diffraction peaks are observed.

The evolution of FWHM and integrated intensity of the selected ND peaks during deformation are shown in Fig. 6. All the peaks exhibit similar evolution; therefore only {111} and {220} grain families were selected for better clarity in the axial direction. In the initial stage of deformation, the broadening of the peaks in the annealed specimen increases, while it significantly decreases in the as-built sample (Fig. 6). The broadening of the peak is a result of substantial increase in dislocation density during plastic deformation in the annealed specimen. Conversely, in the as-built sample during the elastic loading, the steep RS gradients are equalized and hence the diffraction peaks become sharper during the initial stage of the deformation. This process also explains the non-elastic work hardening before the yield point. After the equalization of the RS, the broadening is nearly the same for the annealed and as-built samples, suggesting that there is no significant difference in the evolution of dislocation density during loading in both samples. This is supported by the data from the transverse direction. The peak broadening due to the RS is also present; however, it is not as significant as for the axial direction. After the equalization of the RS inside the sample, it is again possible to observe a similar evolution of peak broadening for the annealed and as-built samples. The texture evolution represented by the evolution of integrated intensity exhibits behavior typical of fcc metals during tensile deformation, i.e., formation of {111} texture at the expense of the {220} component.[58] This evolution of texture was confirmed by EBSD, not shown here. The pronounced plastic deformation and dislocation activity in the annealed specimen is in good agreement with the AE data (Fig. 4) and also with the observed abrupt change in the evolution of lattice strain shown in Fig. 5.

CONCLUSION

It has been shown how in situ ND, together with AE, reveals the deformation behavior of as-built and annealed additively manufactured Alloy 718 samples based on the knowledge of the phase fractions of relevant precipitates from synchrotron XRD and scanning electron microscopy. Upon deformation under tensile loading in the build direction, it was observed that the as-built material is more ductile while the annealed material is stronger. Despite the fact that ND cannot directly resolve the lattice strain in the precipitates, the requirement of load

The Effect of γ'' and δ Phase Precipitation on the Mechanical Properties of Inconel 718 Manufactured by
Selective Laser Melting: An In Situ Neutron Diffraction and Acoustic Emission Study

231

balance in the matrix can indirectly unveil the role of the precipitates in the mechanical behavior of the material. Thus, it could be concluded that the needle-shaped δ precipitates that formed during annealing, entirely consuming the γ'' phase of the as-built state, must carry significant load, shed by the γ matrix of the annealed specimen. This is further supported by the strong AE signal, which is associated with the interaction of δ phase with dislocations.

In contrast, it was found that the γ'' precipitates in the as-built condition most likely do not carry as much load. The presence of coherent γ'' precipitates results in less dislocation-precipitate interaction, due to coherency, which is supported by a low AE signal.

ACKNOWLEDGEMENTS

CONFLICT OF INTEREST

On behalf of all authors, the corresponding author states that there is no conflict of interest.

OPEN ACCESS

REFERENCES

1. E.A. Loria, *JOM* 40, 36 (1988).
2. I. Kirman and D. Warrington, *J. Inst. Met.* 99, 197 (1971).
3. M. Sundararaman, P. Mukhopadhyay, and S. Banerjee, *MTA* 19, 453 (1988).
4. S. Azadian, L.-Y. Wei, and R. Warren, *Mater. Charact.* 53, 7 (2004).
5. H. Li, S. Feng, J. Li, and J. Gong, *Mater. Corros.* 69, 1350 (2018).
6. M. Anderson, A.-L. Thielin, F. Bridier, P. Bocher, and J. Savoie, *Mater. Sci. Eng., A* 679, 48 (2017).
7. J. Gordine, *Weld. J.* 50, 480 (1971).
8. C. Radhakrishna and K. PrasadRao, *J. Mater. Sci.* 32, 1977 (1997).
9. W.E. Frazier, *J. Mater. Eng. Perform.* 23, 1917 (2014).
10. K.N. Amato, S.M. Gaytan, L.E. Murr, E. Martinez, P.W. Shindo, J. Hernandez, S. Collins, and F. Medina, *Acta Mater.* 60, 2229 (2012).
11. Q. Jia and D. Gu, *J. Alloys Compd.* 585, 713 (2014).
12. Q. Jia and D. Gu, *Opt. Laser Technol.* 62, 161 (2014).
13. Y. Lu, S. Wu, Y. Gan, T. Huang, C. Yang, L. Junjie, and J. Lin, *Opt. Laser Technol.* 75, 197 (2015).
14. V.A. Popovich, E.V. Borisov, A.A. Popovich, VSh Sufiiarov, D.V. Masaylo, and L. Alzina, *Mater. Des.* 114, 441 (2017).
15. V.A. Popovich, E.V. Borisov, A.A. Popovich, VSh Sufiiarov, D.V. Masaylo, and L. Alzina, *Mater. Des.* 131, 12 (2017).
16. X. Wang and K. Chou, *JOM* 69, 402 (2017).
17. S. Holland, X. Wang, J. Chen, W. Cai, F. Yan, and L. Li, *J. Alloys Compd.* 784, 182 (2019).
18. T. Raza, J. Andersson, and L.-E. Svensson, *Procedia Manuf.* 25, 450 (2018).
19. D. Zhang, W. Niu, X. Cao, and Z. Liu, *Mater. Sci. Eng., A* 644, 32 (2015).
20. E. Chlebus, K. Gruber, B. Kuźnicka, J. Kurzac, and T. Kurzynowski, *Mater. Sci. Eng., A* 639, 647 (2015).
21. W.M. Tucho, P. Cuvillier, A. Sjolyst-Kverneland, and V. Hansen, *Mater. Sci. Eng., A* 689, 220 (2017).
22. S. Raghavan, B. Zhang, P. Wang, C.-N. Sun, M.L.S. Nai, T. Li, and J. Wei, *Mater. Manuf. Process.* 32, 1588 (2017).
23. Y.-L. Kuo, T. Nagahari, and K. Kakehi, *Materials (Basel)* 2018, 11 (2018).
24. G.H. Cao, T.Y. Sun, C.H. Wang, X. Li, M. Liu, Z.X. Zhang, P.F. Hu, A.M. Russell, R. Schneider, D. Gerthsen, Z.J. Zhou, C.P. Li, and G.F. Chen, *Mater. Charact.* 136, 398 (2018).
25. N. Schell, A. King, F. Beckmann, T. Fischer, M. Müller, and A. Schreyer, *MSF* 772, 57 (2013).
26. M. Drakopoulos, T. Connolley, C. Reinhard, R. Atwood, O. Magdysyuk, N. Vo, M. Hart, L. Connor, B. Humphreys, G. Howell, S. Davies, T. Hill, G. Wilkin, U. Pedersen, A. Foster, N. De Maio, M. Basham, F. Yuan, and K. Wanelik, *J. Synchrotron Rad.* 22, 828 (2015).
27. U. Stuhr, H. Spitzer, J. Egger, A. Hofer, P. Rasmussen, D. Graf, A. Bollhalder, M. Schild, G. Bauer, and W. Wagner, *Nucl. Instrum. Methods Phys. Res. Sect. A Accelerat. Spectrom. Detect. Assoc. Equip.* 545, 330 (2005).
28. U. Stuhr, M. Grosse, and W. Wagner, *Mater. Sci. Eng., A* 437, 134 (2006).
29. O. Arnold, J.C. Bilheux, J.M. Borreguero, A. Buts, S.I. Campbell, L. Chapon, M. Doucet, N. Draper, R. Ferraz, M.A. Gigg, V.E. Lynch, A. Markvardsen, D.J. Mikkelson, R.L. Mikkelson, R. Miller, K. Palmen, P. Parker, G. Passos, T.G. Perring, P.F. Peterson, S. Ren, M.A. Reuter, A.T. Savici, J.W. Taylor, R.J. Taylor, R. Tolchenov, W. Zhou, and J. Zikovsky, *Nucl. Instrum. Methods Phys. Res. A* 764, 156 (2014).
30. V. Dyadkin, P. Pattison, V. Dmitriev, and D. Chernyshov, *J. Synchrotron Rad.* 23, 825 (2016).
31. B.H. Toby and R.B. Von Dreele, *J. Appl. Cryst.* 46, 544 (2013).
32. Y.-L. Kuo, S. Horikawa, and K. Kakehi, *Mater. Des.* 116, 411 (2017).
33. Z. Wang, K. Guan, M. Gao, X. Li, X. Chen, and X. Zeng, *J. Alloys Compd.* 513, 518 (2012).

34. Y. Wang, J. Shi, and Y. Liu, *J. Cryst. Growth* 521, 15 (2019).
35. M. Ni, C. Chen, X. Wang, P. Wang, R. Li, X. Zhang, and K. Zhou, *Mater. Sci. Eng., A* 701, 344 (2017).
36. M. Calandri, S. Yin, B. Aldwell, F. Calignano, R. Lupoi, and D. Ugues, *Materials (Basel)* 2019, 12 (2019).
37. F. Brenne, A. Taube, M. Pröbstle, S. Neumeier, D. Schwarze, M. Schaper, and T. Niendorf, *Prog. Addit. Manuf.* 1, 141 (2016).
38. C.R. Heiple and S.H. Carpenter, *J. Acoust. Emiss.* 6, 177 (1987).
39. H. Yu, S. Hayashi, K. Kakehi, and Y.-L. Kuo, *Metals* 9, 19 (2019).
40. J.F. Shackelford, Y.-H. Han, S. Kim, S.-H. Kwon, Y.-H. Han, S. Kim, and S.-H. Kwon, *CRC Materials Science and Engineering Handbook* (Boca Raton: CRC Press, 2016).
41. S.S.-Y. Hsu and K. Ono, in *The Proceedings of the 6th International Acoustic Emission Symposium* (Susono City, Japan, 1982), p. 12.
42. A. Arieli, R.P. Wells, M.A. Hamstad, and A.K. Mukherjee, *Mech. Mater.* 2, 1 (1983).
43. Z. Chen, R.L. Peng, J. Moverare, P. Avdovic, J.M. Zhou, and S. Johansson, *Metall. Mater. Trans. A* 47, 3664 (2016).
44. J.M. Oblak, D.F. Paulonis, and D.S. Duvall, *MT* 5, 143 (1974).
45. M.C. Chaturvedi and Y. Han, *Met. Sci.* 17, 145 (1983).
46. D.C. Lv, D. McAllister, M.J. Mills, and Y. Wang, *Acta Mater.* 118, 350 (2016).
47. D. McAllister, D. Lv, B. Peterson, H. Deutchman, Y. Wang, and M.J. Mills, *Scripta Mater.* 115, 108 (2016).
48. D.-X. Wen, Y.C. Lin, J. Chen, X.-M. Chen, J.-L. Zhang, Y.-J. Liang, and L.-T. Li, *J. Alloys Compd.* 618, 372 (2015).
49. Y. Mu, C. Wang, W. Zhou, and L. Zhou, *Metals* 8, 86 (2018).
50. T. Jayakumar, B. Raj, D.K. Bhattacharya, P. Rodriguez, and O. Prabhakar, *Mater. Sci. Eng., A* 150, 51 (1992).
51. W.F. Hosford, *Mechanical Behavior of Materials*, 2nd ed. (Cambridge: Cambridge University Press, 2009).
52. M.R. Daymond, M.A.M. Bourke, R.B. Von Dreele, B. Clausen, and T. Lorentzen, *J. Appl. Phys.* 82, 1554 (1997).
53. J. Repper, P. Link, M. Hofmann, C. Krempaszky, W. Petry, and E. Werner, *Appl. Phys. A* 99, 565 (2010).
54. H.Y. Zhang, S.H. Zhang, M. Cheng, and Z.X. Li, *Mater. Charact.* 61, 49 (2010).
55. D.-G. He, Y.C. Lin, L.-H. Wang, Q. Wu, Z.-H. Zu, and H. Cheng, *Vacuum* 161, 242 (2019).
56. B. Vrancken, V. Cain, R. Knutsen, and J. Van Humbeeck, *Scripta Mater.* 87, 29 (2014).
57. B. Ahmad, S.O. van der Veen, M.E. Fitzpatrick, and H. Guo, *Addit. Manuf.* 22, 571 (2018).
58. S. Van Petegem, J. Wagner, T. Panzner, M.V. Upadhyay, T.T.T. Trang, and H. Van Swygenhoven, *Acta Mater.* 105, 404 (2016).